





## Article

# Highly Efficient Photothermal Reduction of CO<sub>2</sub> on Pd<sub>2</sub>Cu Dispersed TiO<sub>2</sub> Photocatalyst and Operando DRIFT Spectroscopic Analysis of Reactive Intermediates

Munirathinam Elavarasan <sup>1</sup>, Willie Yang <sup>2</sup>, Sethupathi Velmurugan <sup>3</sup>, Jyy-Ning Chen <sup>1</sup>, Thomas C.-K. Yang <sup>1,3,\*</sup> and Toshiyuki Yokoi <sup>2,\*</sup>

<sup>1</sup> Department of Chemical Engineering and Biotechnology, National Taipei University of Technology, No. 1, Section 3, Chung-Hsiao East Road, Taipei 106, Taiwan; 2011.elavarasan@gmail.com (M.E.); jingsi229@gmail.com (J.-N.C.)

<sup>2</sup> Institute of Innovative Research, Tokyo Institute of Technology, Yokohama 226-8503, Japan; willie0106@gmail.com

<sup>3</sup> Precision Analysis and Material Research Center, National Taipei University of Technology, No. 1, Section 3, Chung-Hsiao East Road, Taipei 106, Taiwan; sethupathivelmurugan@gmail.com

\* Correspondence: ckyang@mail.ntut.edu.tw (T.C.-K.Y.); yokoi@cat.res.titech.ac.jp (T.Y.)

**Abstract:** The photocatalytic conversion of CO<sub>2</sub> to fuels using solar energy presents meaningful potential in the mitigation of global warming, solar energy conversion, and fuel production. Photothermal catalysis is one promising approach to convert chemically inert CO<sub>2</sub> into value-added chemicals. Herein, we report the selective hydrogenation of CO<sub>2</sub> to ethanol by Pd<sub>2</sub>Cu alloy dispersed TiO<sub>2</sub> (P25) photocatalyst. Under UV-Vis irradiation, the Pd<sub>2</sub>Cu/P25 showed an efficient CO<sub>2</sub> reduction photothermally at 150 °C with an ethanol production rate of 4.1 mmol g<sup>-1</sup> h<sup>-1</sup>. Operando diffuse reflectance infrared Fourier transform (DRIFT) absorption studies were used to trace the reactive intermediates involved in CO<sub>2</sub> hydrogenation in detail. Overall, the Cu provides the active sites for CO<sub>2</sub> adsorption and Pd involves the oxidation of H<sub>2</sub> molecule generated from P25 and C–C bond formation.

**Keywords:** photothermal reactor; CO<sub>2</sub> reduction; photocatalytic H<sub>2</sub>O oxidation; DRIFT; alloy



**Citation:** Elavarasan, M.; Yang, W.; Velmurugan, S.; Chen, J.-N.; Yang, T.C.-K.; Yokoi, T. Highly Efficient Photothermal Reduction of CO<sub>2</sub> on Pd<sub>2</sub>Cu Dispersed TiO<sub>2</sub> Photocatalyst and Operando DRIFT Spectroscopic Analysis of Reactive Intermediates. *Nanomaterials* **2022**, *12*, 332. <https://doi.org/10.3390/nano12030332>

Academic Editor: Vincenzo Vaiano

Received: 14 December 2021

Accepted: 15 January 2022

Published: 21 January 2022

**Publisher's Note:** MDPI stays neutral with regard to jurisdictional claims in published maps and institutional affiliations.



**Copyright:** © 2022 by the authors. Licensee MDPI, Basel, Switzerland. This article is an open access article distributed under the terms and conditions of the Creative Commons Attribution (CC BY) license (<https://creativecommons.org/licenses/by/4.0/>).

## 1. Introduction

An anthropogenic climate dramatically increases the CO<sub>2</sub> level in the atmosphere, which can lead to the deterioration of the environment. The utilization of CO<sub>2</sub> is an alternative route to reduce it in the environment, and it can also be converted into valuable fuels and chemicals [1–5]. The photocatalytic hydrogenation of CO<sub>2</sub> is an efficient technique for eco-friendly conversion, but CO<sub>2</sub> activation and selective hydrogenation remain a challenge [6,7]. This is due to the high thermodynamic stability and chemical inertness of CO<sub>2</sub> [8,9]. Therefore, the activation and hydrogenation of CO<sub>2</sub> require enormous energy to break the O=C=O bond and implement the insertion of the C–H bond. Previous research studies show that the hydrogenation of CO<sub>2</sub> resulted in numerous other products. Mostly, the CO<sub>2</sub> reduction processes resulted in the production of carbon monoxide (CO), a more extremely poisonous gas than CO<sub>2</sub>. Moreover, it is very rare to produce value added chemicals, such as methane, methanol, acids, and hydrocarbons [10–17]. Therefore, the selective hydrogenation of CO<sub>2</sub> to ethanol has received great attention, and this can be achieved via electrochemical and thermochemical processes [18,19]. However, no appreciable development in the field of photo- and photothermal catalysts has been observed, which offers a sustainable method for CO<sub>2</sub> to ethanol conversion.

Currently, palladium (Pd) and platinum (Pt) based catalysts are demonstrated for the selective hydrogenation of CO<sub>2</sub> to ethanol [19–21]. In such processes, the Pd metal is cheaper than Pt, and Pd-based catalysts have worked well in the C–C coupling reactions as

well [22]. Besides, the C–C coupling reaction step is the most important step to control the yield of ethanol [23]. Copper (Cu) is the cheapest and most easily available material, and it has greater affinity for CO<sub>2</sub> gas. Moreover, oxides of Cu represent an efficient photocatalyst with excellent redox potential for water splitting (water oxidation) in the photocatalytic hydrogen evolution reaction [24]. The Cu/Fe<sub>2</sub>O<sub>3</sub> catalyst is a promising catalyst for water-splitting in thermochemical reactions, to produce H<sub>2</sub> and capture CO<sub>2</sub> at the same time [25]. TiO<sub>2</sub> has been proven to be a most promising material in photocatalytic water splitting, pollutant degradation, self-cleaning agents, and many other fields [26,27]. The effect of reaction temperature on photodegradation performance was studied over Pd/TiO<sub>2</sub> and Cu/TiO<sub>2</sub> photocatalysts. The result revealed that Pd/TiO<sub>2</sub> performed well during the photodegradation of methylene blue. [28] Therefore, the combination of two attractive elements is an efficient way to produce ethanol. Previous studies have demonstrated the various combinations of Pd-Cu nanoparticles that are highly selective and active catalysts for the production of ethanol from CO<sub>2</sub> by thermochemical reaction [19]. Although selective hydrogenation produces valuable chemicals, the mechanism behind this selectivity is still an uncovered area. Therefore, the mechanism of selective CO<sub>2</sub> reduction was probed by operando diffuse reflectance infrared Fourier transform absorption spectroscopy (DRIFTS).

The DRIFT study is used to detect the molecules and ions at their place of origin where the chemicals and substances are being produced in a chemical reaction. DRIFT analysis is a widely used technique for in-situ studies concerning the photodegradation of adsorbed dye and tracing the gas adsorbed reaction mechanism on the catalytic surface. It has also been used in agro-food industries due to its analytical compatibility with physicochemical properties of food commodities [29,30]. Moreover, DRIFT analysis was applicable to test non-transparent and indispersable materials. In our previous work, we have demonstrated photocatalytic efficiency and the reaction mechanism using DRIFT in the oxidation of ethanol [31]. The solid-state photodegradation mechanism was evaluated by DRIFT for the surface adsorbed AB-9 dye on titanium dioxide (TiO<sub>2</sub>) [32]. This technique was used to investigate the electron transfer and energy conversion processes at the interface, adsorbed species, and dynamics of photo-generated electrons on nitrogen-doped TiO<sub>2</sub> in dye-sensitized solar cells (DSSC) [33]. Moreover, the DRIFT analysis was used to identify the reaction mechanism of CO<sub>2</sub> hydrogenation [19,20,34].

In this work, we investigate the selective hydrogenation of CO<sub>2</sub> to ethanol by Pd<sub>2</sub>Cu/P25 photocatalyst. A facile one-pot synthesis procedure was used to obtain the Pd<sub>2</sub>Cu alloys on TiO<sub>2</sub> nanoparticles. The physicochemical properties of the as prepared Pd<sub>2</sub>Cu/P25 catalysts were analyzed using various analytical techniques. The hydrogenation of CO<sub>2</sub> was tested using as-prepared Pd<sub>2</sub>Cu/P25 catalysts following the photothermal method. Moreover, the reactive intermediates and reaction mechanism of hydrogenation of CO<sub>2</sub> to ethanol were determined from operando DRIFT analysis.

## 2. Materials and Methods

### 2.1. Chemicals

Palladium (II) bis(acetylacetonate) (Pd(acac)<sub>2</sub>, 99%), Oleylamine (70%), ethyl alcohol (99.9%), and acetone (99.9%) were purchased from Sigma Aldrich. Copper chloride dihydrate (CuCl<sub>2</sub>·2H<sub>2</sub>O, 99%), triphenylphosphine (TPP, 99%), and commercial P25 (99.9% grade) were obtained from Nacalai Tesque, Acros Organics, and Degussa, respectively. The gases deployed in this research, such as high purity nitrogen (N<sub>2</sub>, 99.999%), carbon dioxide (CO<sub>2</sub>, 99.5%), and helium (He, 99.99%), were procured from Yusheng gas company, Taipei, Taiwan.

### 2.2. Preparation of Pd<sub>2</sub>Cu/P25 Photocatalyst

For the synthesis of Pd<sub>2</sub>Cu/P25 photocatalyst, 10 mg of Pd(acac)<sub>2</sub> and 55 mg of CuCl<sub>2</sub>·2H<sub>2</sub>O were dissolved in 12 mL of Oleylamine in a three-neck flask. Additionally, 90 mg of triphenylphosphine (TPP) was added. The flask was heated to 80 °C under continuous stirring in an N<sub>2</sub> atmosphere for about 20 min until the chemicals were thoroughly

dissolved. The temperature was then gradually raised to 170 °C, and the system was kept at this temperature for 4 h. Then, 100 mg of TiO<sub>2</sub> (P25) was added to this suspension and kept for 20 min, before being naturally cooled down to room temperature. The precipitate was separated and washed with a mixture of ethyl alcohol and acetone. The obtained precipitate dried overnight at 85 °C, followed by calcination at 450 °C for 4 h.

### 2.3. DRIFT Analysis

The DRIFT experiments were conducted by Perkin Elmer FT-IR spectroscopy. The custom-designed Harrick DRIFT cell was utilized for this study. Approximately 40 mg of the photocatalyst was placed in a DRIFT cell sample holder. The sample was covered by ZnSe/CaF<sub>2</sub> windows for IR radiation and a light source was passed through respectively. The DRIFT chamber was filled with N<sub>2</sub> gas for 20 min to remove impurities, before the background spectrum of the sample was acquired. The temperature of the sample was controlled using a thermocouple attached to the DRIFT cell. The wavenumber resolution was fixed at 4 cm<sup>-1</sup>, and the experiments were carried out in the range of 500–4000 cm<sup>-1</sup>. For the CO<sub>2</sub> reduction experiment, the CO<sub>2</sub> was purged into the chamber with the water vapor at 10 cc/s for 120 min. An outlet of the reaction chamber was connected with the mass spectrum during the collection of DRIFT spectra. Meanwhile, the mass spectra were also collected (QMS 100 Series, capillary; PEEK, and glass-lined plastic inlet type, pressure 10 mbar to 1 bar, Quadrupole type spectrometer, Faraday cup standard electron multiplier optional detector) [31].

### 2.4. Photothermal CO<sub>2</sub> Reduction by the Reactor

The photothermal CO<sub>2</sub> reduction was performed in a custom-made reactor. Firstly, 40 mg of Pd<sub>2</sub>Cu/P25 was dispersed in 50 mL of deionized (DI) water by ultrasonicator, then poured into the reactor. Therein, the magnetic stirrer continuously stirred the dispersion. Subsequently, the CO<sub>2</sub> was purged into the reactor and saturated for 30 min, and then the reactor was closed perfectly. The UV-Vis (350 to 750 nm) light source (with an intensity of 380.8 μW) was used to irradiate the reactor. The reaction was kept at 80 °C by the hotplate. During each measurement, 0.1 μL of the reaction mixture was collected from the reaction and analyzed by gas chromatography (GC Model 6890 N/MS Model 5973, Agilent Technologies, Poway, CA, USA).

### 2.5. Characterizations

The crystal structures of the as-prepared samples were investigated by the X-ray diffractometer (XRD) with Cu-Kα radiation ( $\lambda = 1.5406 \text{ \AA}$ ). The Raman spectra and UVDRS spectra of the samples were recorded using confocal Raman spectroscopy (ACRON Technology, Taipei, Taiwan) and UV-Vis-NIR spectroscopy (Agilent Technology, Santa Clara, CA, USA), respectively. The back scattered images of the as-synthesized samples were recorded by scanning electron microscopy (FESEM, JEOL-JSM-7610F, Tokyo, Japan). High-resolution transmission electron microscopy (HRTEM) images were obtained from JEOL TEM (JEM-2010) at 200 kV. The element composition was recorded on the energy dispersive spectrum EDS (HORIBA, X-act, Tokyo, Japan). The JEOL JPS-9030 (Tokyo, Japan) X-ray photoelectron spectrometer (XPS) was deployed to analyze the surface properties of the prepared samples. The dissolved solution of the as prepared photocatalyst was analyzed by the inductively coupled plasma-atomic emission spectrometer (ICP-AES, Shimadzu ICPE-9000, Kyoto, Japan) for the quantitative elemental contents in each sample.

### 2.6. Dark Adsorption by CO<sub>2</sub> with Transmission FTIR

The dark adsorption experiment was carried out in the transmission mode by a spectrometer (JASCO FT-IR 4600, Tokyo, Japan) equipped with a Mercury Cadmium Telluride detector. The sample was pressed into a self-supporting disk (20 mm diameter, ca. 30 mg) and placed in an IR cell attached to a gas-phase closed circulatory system for observation. The sample was pretreated at 723 K for 1 h under vacuum and then probed

by a fixed amount of CO<sub>2</sub> vapor from 5 to 500 Pa at ambient temperature. After the dark adsorption at 500 Pa, the system was evacuated to vacuum again to remove free CO<sub>2</sub> and other free carbonyl species, to investigate the chemically adsorbed CO<sub>2</sub> species on the samples.

### 3. Results and Discussion

#### 3.1. Material Characterizations

Figure 1a shows the X-ray diffraction patterns of Pd<sub>2</sub>Cu alloy on P25 along with the diffraction pattern of pristine P25. The observed crystalline peaks at 41.11, 48.46, and 71.02° are attributed to the (111), (200), and (220) planes of PdCu alloy that are matched with the ICDD No. 00-048-1551 [35]. The obtained crystalline parameters indicate that the Pd<sub>2</sub>Cu alloy is crystallized in the body-centered cubic crystal. The crystal structure of Pd<sub>2</sub>Cu is illustrated in the inset of Figure 1a.

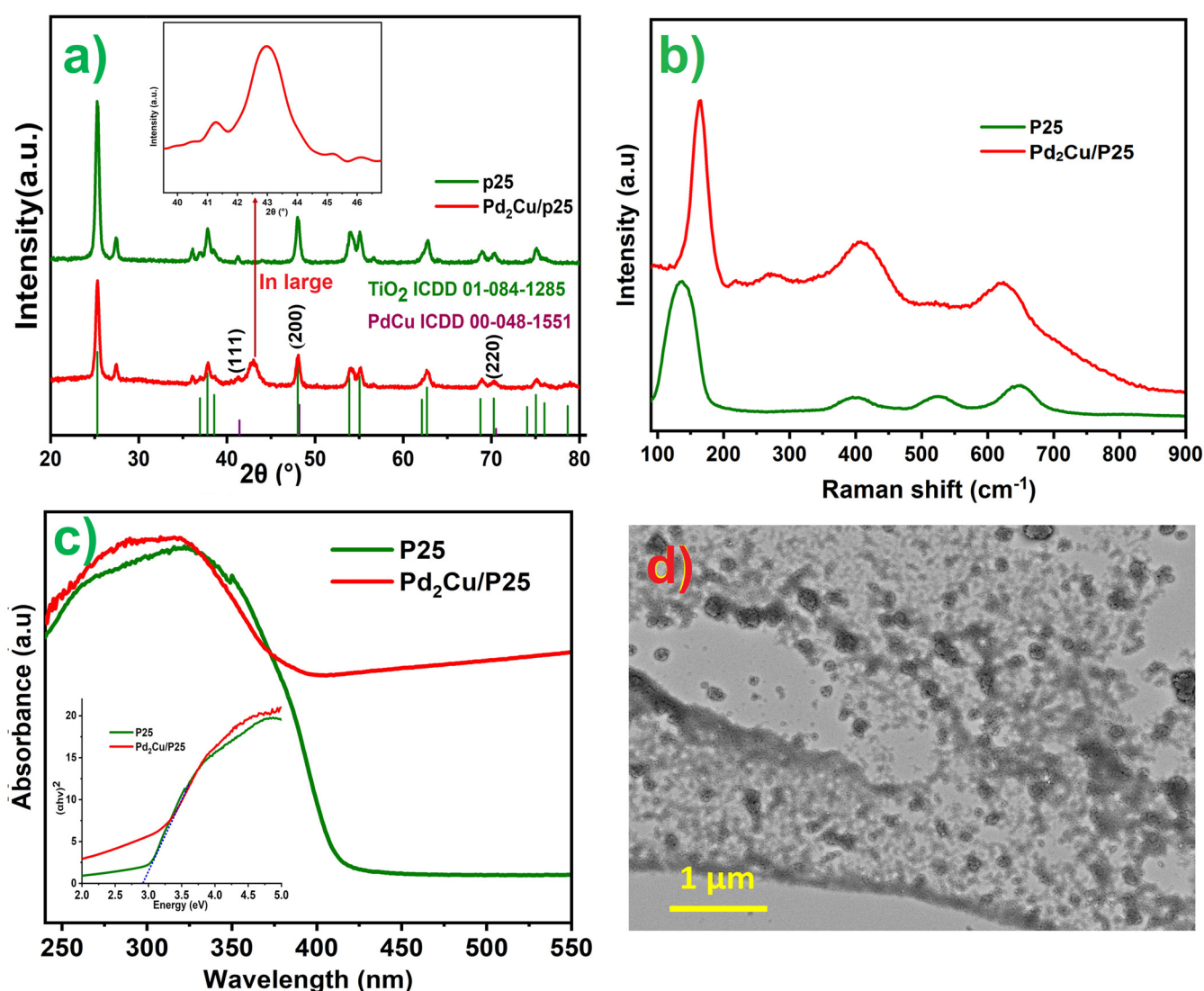


**Figure 1.** (a) XRD pattern, (b) Raman spectra (c) UV–Vis (DRS), inset is showing Tauc plots of P25 and Pd<sub>2</sub>Cu/P25, (d) FESEM Backscattered–Electron (BSE) Image of Pd<sub>2</sub>Cu/P25.

Moreover, the remaining peaks at 25.38, 38.23, 48.47, 54.71, 56.01, 27.58, 36.90, 41.60, and 55.0° are assigned to the (101), (004), (200), (105), (211), (110), (101), (210), and (211) planes of TiO<sub>2</sub> (P25) respectively [31]. It can be seen from XRD peaks that the intensities of Pd<sub>2</sub>Cu peaks are dominated by the P25 crystalline peaks. This is because of the low

loading level and high dispersion of Pd<sub>2</sub>Cu on P25. Figure 1b shows the Raman spectra of Pd<sub>2</sub>Cu/P25 and P25. The typical peaks appearing at 142, 397, 533, and 651 cm<sup>-1</sup> correspond to the Eg, B1g, A1g, and Eg modes of TiO<sub>2</sub> (P25), respectively. The additional peaks that appeared at 218 and 279 cm<sup>-1</sup> are correlated to the specific interactions between PdCu alloys and P25. The PdCu alloys have no vibrations. However, the corresponding oxides of Pd and Cu revealed significant peaks. The vibrations at 398 and 650 cm<sup>-1</sup> are increased for the Pd<sub>2</sub>Cu/P25 when compared with P25. This might be attributed to the stretching vibrations of Pd-O and Cu-O. Moreover, the light absorption properties of Pd<sub>2</sub>Cu/P25 were investigated by UV-Vis spectra. As shown in Figure 1c, the UV-visible absorption spectra of Pd<sub>2</sub>Cu/P25 exhibited stronger absorption in the visible range when compared to the P25. The indirect bandgap of Pd<sub>2</sub>Cu/P25 is estimated from the plots of  $(\alpha h\nu)^{1/2}$  vs.  $h\nu$  (energy of light), which shows 3.0 eV for both Pd<sub>2</sub>Cu/P25 and P25 (Figure 1c, inset). Furthermore, the FESEM backscattered electron (BSE) image gives the topography of the P25 supported Pd<sub>2</sub>Cu alloys.

Figure 1d shows the BSE image of Pd<sub>2</sub>Cu/P25, wherein the Pd<sub>2</sub>Cu alloy shows a stronger backscatter electron signal, which can be seen as dark spots. P25 exhibits a weaker electron signal. This BSE image can help to distinguish the Pd<sub>2</sub>Cu alloy and P25 in the highly dispersed Pd<sub>2</sub>Cu/P25 catalyst. Figure 2a displays the TEM images of Pd<sub>2</sub>Cu alloy on the P25 nanoparticles, wherein the 5 ± 1 nm-sized Pd<sub>2</sub>Cu nanodots are highly dispersed on 20 ± 5 nm-sized P25 nanoparticles. The high magnification images (Figure 2b,c) clearly show the mono dispersion of Pd<sub>2</sub>Cu nanodots and their lattice fringes (Figure 2d). Figure 2e shows the SAED patterns of Pd<sub>2</sub>Cu/P25, which are taken at a random angle to view clear ED patterns. The obtained ring patterns are indexed to the (101), (200), and (111), (311) planes, which are in accordance with the XRD patterns of P25 and Pd<sub>2</sub>Cu, respectively. The uniform distribution and the ratio of elemental percentage are investigated using the EDX and mapping studies. Figure 2f reveals 82% of P25 and 18% of Pd<sub>2</sub>Cu alloy in the photocatalyst, respectively. Moreover, elemental mapping of Pd<sub>2</sub>Cu/P25 was performed and the results are shown in Figure 2g-j. Thus, it confirmed that the Pd<sub>2</sub>Cu nanodots are uniformly distributed on the P25 nanoparticles, supporting better photothermal CO<sub>2</sub> conversion.

The X-ray photoelectron spectra (XPS) were used to explore the surface properties of Pd<sub>2</sub>Cu/P25. The narrow scan Pd 3d spectrum shows two peaks for spin-orbits 3d<sub>5/2</sub> and 3d<sub>3/2</sub> at 339 and 345 eV, corresponding to the metallic Pd<sup>0</sup> respectively (Figure 3a). Moreover, the deconvolution spectra of Pd 3d show an additional peak for the Pd<sup>2+</sup>, which is attributed to PdO on the surface [36]. Figure 3b shows the narrow scan spectrum of Cu 2p. The binding energies at 937 and 957 eV correspond to the 2p<sub>3/2</sub> and 2p<sub>1/2</sub> spin-orbits, respectively. The Cu 2p spectrum was deconvoluted into four peaks. The two main peaks denote Cu in the metallic state, while the minor peaks denote Cu in +2 oxidation states. Similar to Pd, Cu also exhibited CuO on its surface. Moreover, the peak intensity of Cu 2p was lower than that of Pd, which is in accordance with EDX results. Additionally, Figure 3c,d shows the narrow scan peaks of Ti 2p and O 1s, which are indexed to the typical peaks of TiO<sub>2</sub> (P25). The Ti 2p spectra shows two peaks at the binding energies of 462.1 and 467.8 eV belonging to the 2p<sub>3/2</sub> and 2p<sub>1/2</sub> orbitals, respectively. The deconvoluted O 1s peak reveals two binding energies at 533.5 and 535.3 eV, corresponding to the surface hydroxyl groups and lattice oxygen atoms respectively. Overall, these characterizations confirm the formation of Pd<sub>2</sub>Cu alloy on the P25 support. The amount of metals proportion in the photocatalyst were further confirmed by ICP-AES. For the analysis, the powder of the as-prepared catalyst was soaked in the aqua regia solutions for 6 hours and then mixed with 30wt% HF for overnight. The results were summarized in Table 1.

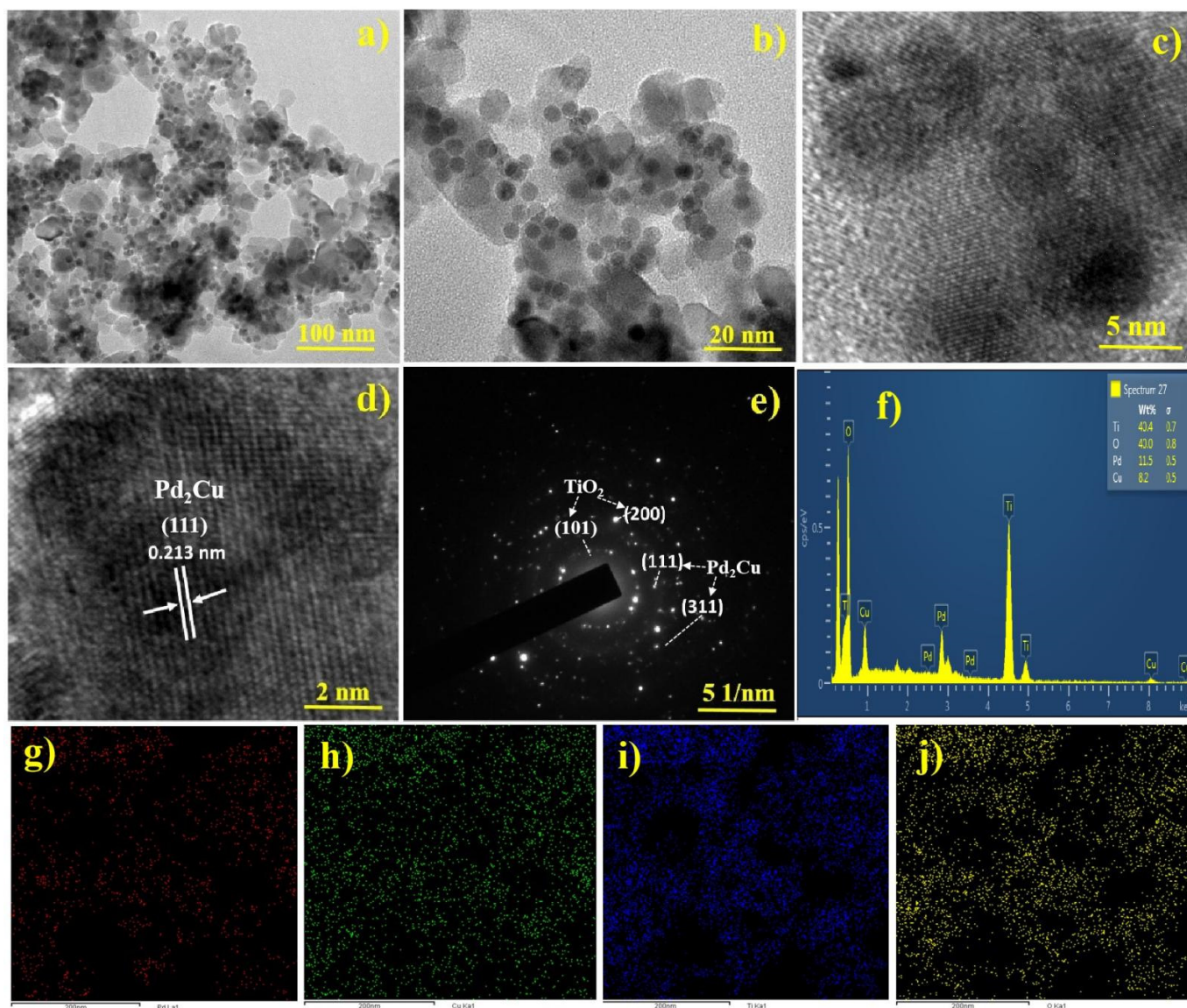


**Figure 2.** (a–c) low and high magnified TEM images, (d) lattice fringes, (e) SAED patterns, (f) EDX spectra, (g–j) mapping of Pd<sub>2</sub>Cu/P25 (Elements: Pd (g); Cu (h); Ti (i); O (j)).

**Table 1.** ICP-AES results of Pd<sub>2</sub>Cu/P25 photocatalyst.

ICP Analysis	Pd	Cu	Ti
mg L <sup>-1</sup>	0.0416	0.0129	0.232
Molecular Weight	106.42	63.54	47.867
mMOLL <sup>-1</sup>	$3.9 \times 10^{-4}$	$2.0 \times 10^{-4}$	$4.8 \times 10^{-3}$
Molar ratios	~2	1	24

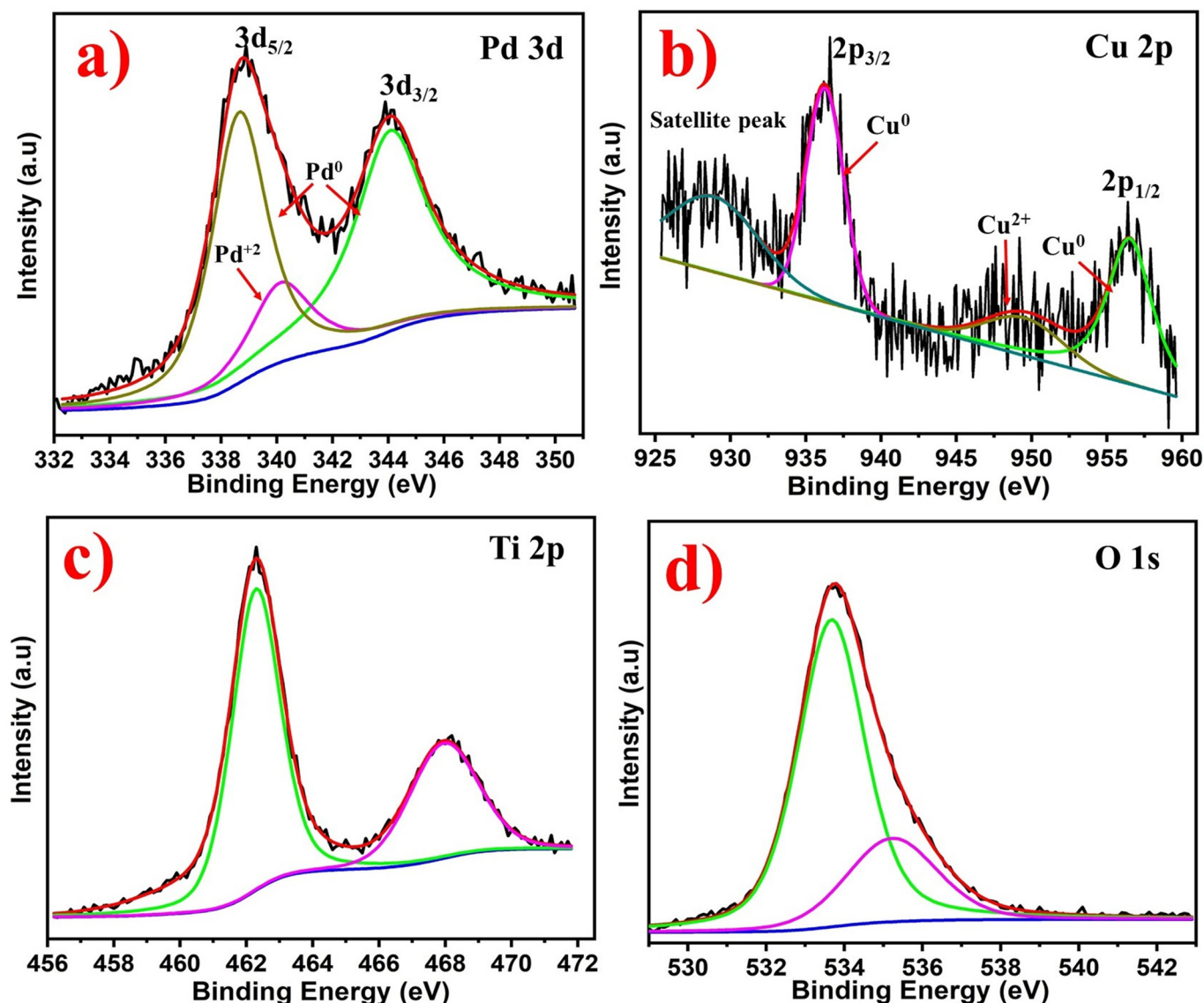
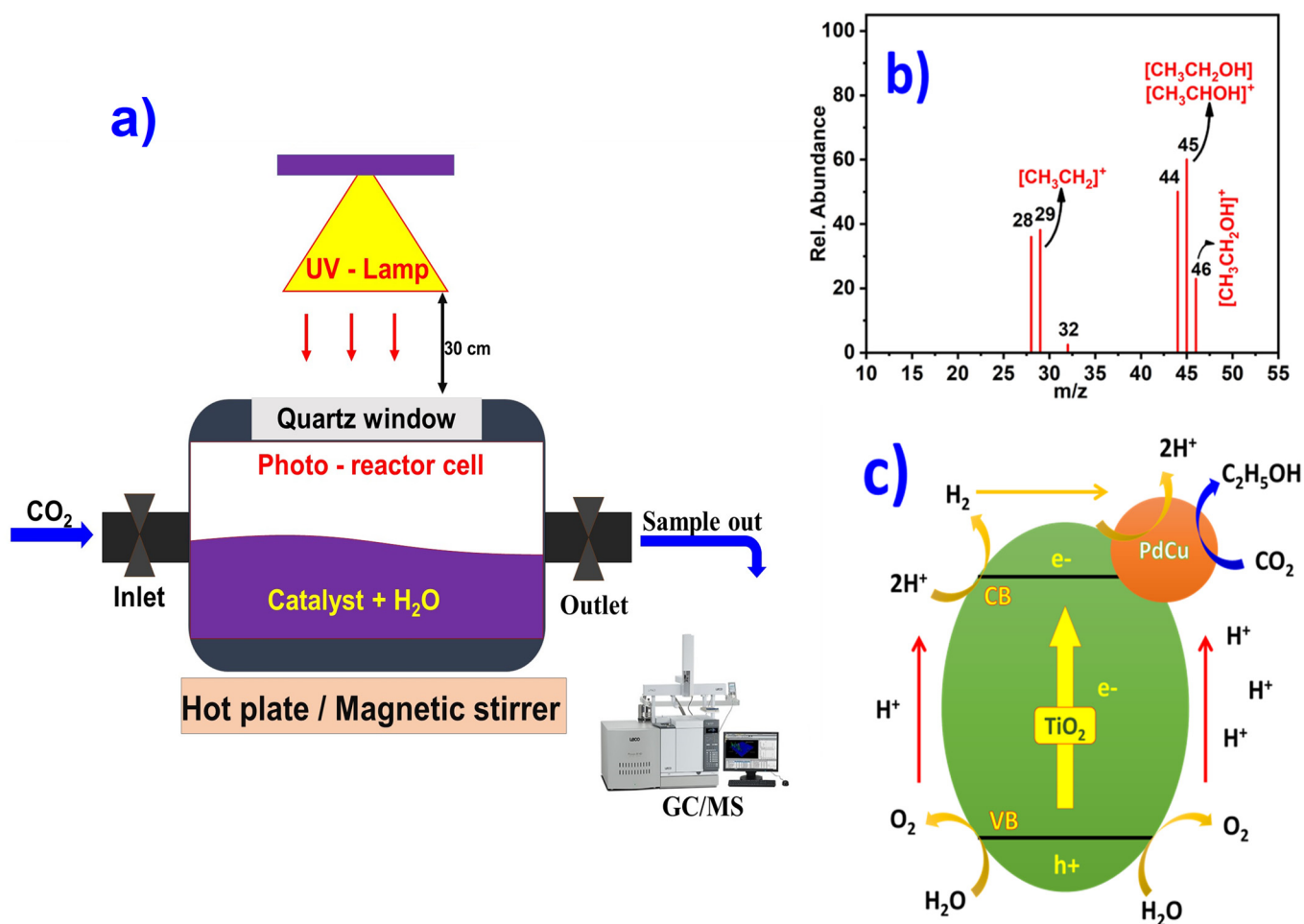


Figure 3. (a) Pd 3d, (b) Cu 2p, (c) Ti 2p, and (d) O 1s XPS spectra of Pd<sub>2</sub>Cu/P25.

### 3.2. Photothermal CO<sub>2</sub> Reduction

The photothermal hydrogenation of CO<sub>2</sub> over a Pd<sub>2</sub>Cu/P25 catalyst was evaluated using the photoreactor. The detailed experimental procedure is presented in the experimental section and the schematic diagram of the reactor setup is shown in Figure 4a. The reaction was continued for up to six hours, while the sample was taken from the reaction mixture and subjected to the GCMS analysis. In the first hour, no products were seen in the reaction mixture. Afterwards, the GCMS shows the peaks for ethanol, as shown in Figure 4b. The typical fragmentation of mass 45 and 46 m/z correspond to the [C<sub>2</sub>H<sub>5</sub>O]<sup>+</sup> and [C<sub>2</sub>H<sub>5</sub>OH]<sup>+</sup> respectively [37]. The ethanol yield is shown in Table 2, and the yield was compared with other reported catalysts. The photocatalytic CO<sub>2</sub> reduction of Pd<sub>2</sub>Cu/P25 was also compared with pristine P25. The P25 showed no signal for ethanol production. Herein, the P25 (TiO<sub>2</sub>) oxidized the water at its valence band, and the electrons were utilized by Pd<sub>2</sub>Cu at the conduction band. Further, the Pd<sub>2</sub>Cu has reduced the CO<sub>2</sub> by capturing the H<sup>+</sup> from aqueous media. Therefore, without Pd<sub>2</sub>Cu, it is difficult to produce ethanol by P25 alone. Figure 4c shows the schematic representation of the overall reaction process. Furthermore, the reaction mechanism of CO<sub>2</sub> reduction and the intermediate products were explored by the DRIFT analysis.



**Figure 4.** (a) Schematic diagram of photothermal CO<sub>2</sub> reduction using photoreactor, (b) GCMS spectrum of ethanol after 1h UV-Vis light irradiation at 80 °C. (c) The overall process of CO<sub>2</sub> reduction and H<sub>2</sub>O oxidation on Pd<sub>2</sub>Cu/P25 (CB: conduction band, VB: valence band, h<sup>+</sup>: holes, and e<sup>-</sup>: electrons).

**Table 2.** The comparison of ethanol yield on Pd<sub>2</sub>Cu/P25 with various catalysts.

Catalysts	Gas (CO <sub>x</sub> )	Temperature (°C)	C <sub>2</sub> H <sub>5</sub> OH Yields (mmol g <sup>-1</sup> h <sup>-1</sup> )	Reference
1% Pt/Co <sub>3</sub> O <sub>4</sub>	CO <sub>2</sub>	200	0.07	[38]
1.2% RhMnLiFe	CO	320	3.5	[39]
Rh/SiO <sub>2</sub>	CO	250	0.37	[40]
Au/TiO <sub>2</sub>	CO <sub>2</sub>	200	2.82	[41]
8.7% Pd-10% Cu/SiO <sub>2</sub>	CO <sub>2</sub>	250	1.12	[42]
Pd <sub>2</sub> Cu/P25	CO <sub>2</sub>	150	4.1	This work

### 3.3. The FTIR Spectra of the Dark Adsorption of CO<sub>2</sub> on Photocatalysts

An airtight gas-cell FTIR accessory with 15 cm pathlength for transmission mode measurements was used to analyze the extent of interactions between adsorbates and photocatalysts. Figure 5 illustrates the FTIR spectra of Pd<sub>2</sub>Cu/P25 probed by CO<sub>2</sub> from 5 to 500 Pa at ambient temperature. After the CO<sub>2</sub> adsorption at 500 Pa was completed, the system was evacuated to vacuum again to remove the free CO<sub>2</sub> and free carbonate species. The evacuated spectrum is symbolized as “Evac.” in Figure 5. This information provides strong evidence of the formation of chemical adsorption bonding between our sample and carbonate species. The peaks are assigned following the reference [43–47]. These spectra feature two major species, namely carbonates and bicarbonates, that were



adsorbed on the catalysts by a few different kinds of connections. Starting with bicarbonates, the band at  $1215\text{ cm}^{-1}$  is related to the (OH) vibrational signals of monodentate and bidentate bicarbonates ( $m\text{-HCO}_3^-$  and  $b\text{-HCO}_3^-$ ). The band at around  $1625\text{ cm}^{-1}$  can be ascribed to the asymmetric vibrational signals ( $\nu_{\text{as}}(\text{CO}_3)$ ) of both monodentate and bidentate bicarbonates ( $m\text{-HCO}_3^-$  and  $b\text{-HCO}_3^-$ ) [43–46]. However, the significant bands at  $1425\text{ cm}^{-1}$ , identified as the symmetric vibration signal ( $\nu_{\text{s}}(\text{CO}_3)$ ) of the bidentate bicarbonates ( $b\text{-HCO}_3^-$ ), implies that the bicarbonate groups on the  $\text{Pd}_2\text{Cu}/\text{P25}$  were dominated by bidentate bicarbonates ( $b\text{-HCO}_3^-$ ).

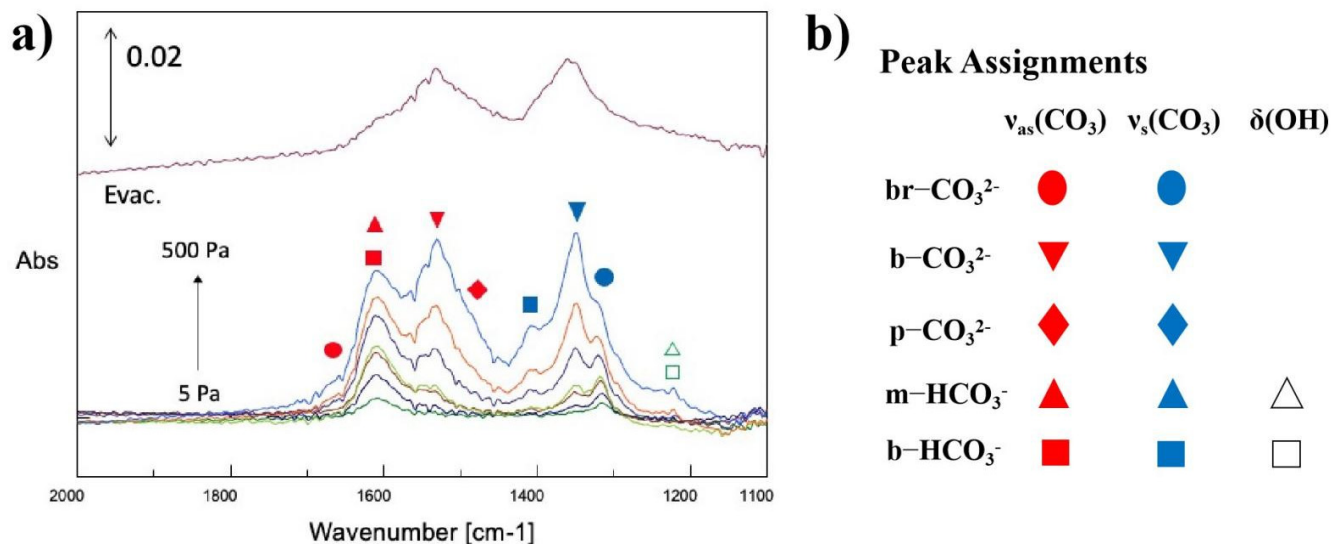


**Figure 5.** (a) The FTIR spectra of the dark adsorption on the  $\text{Pd}_2\text{Cu}/\text{P25}$  photocatalysts and (b) peak assignments at various pressure gradients from 5 Pa to 500 Pa of  $\text{CO}_2$  vapor and finally in vacuum condition.

The bands related to carbonate species were also investigated. The broad bands at  $1675\text{ cm}^{-1}$  and  $1325\text{ cm}^{-1}$  represented the asymmetric vibrational signals ( $\nu_{\text{as}}(\text{CO}_3)$ ) and the symmetric vibration signal ( $\nu_{\text{s}}(\text{CO}_3)$ ) of the adsorbed bridged carbonates ( $\text{br-CO}_3^{2-}$ ), respectively [43–46]. The significant bands at  $1525\text{ cm}^{-1}$  and  $1350\text{ cm}^{-1}$  exhibited the asymmetric vibrational signals ( $\nu_{\text{as}}(\text{CO}_3)$ ) and the symmetric vibration signal ( $\nu_{\text{s}}(\text{CO}_3)$ ) of the adsorbed bidentate carbonates ( $\text{b-CO}_3^{2-}$ ), respectively. Besides, a small shoulder at  $1500\text{ cm}^{-1}$  (asymmetric vibrational signals ( $\nu_{\text{as}}(\text{CO}_3)$ )) indicated that there was a trace amount of poly-dentate carbonate species ( $\text{p-CO}_3^{2-}$ ) observed by IR. After the sample reached equilibrium at 500 Pa of  $\text{CO}_2$ , the system was then turned in to vacuum for 30 min. As shown in Figure 5, the remaining signals mostly belonged to carbonates. This result can provide further insights in DRIFT analysis when the reaction was applied.

Thus, the dark adsorption FTIR analysis probed by  $\text{CO}_2$  was carried out using  $\text{Pd}_2\text{Cu}/\text{P25}$ . This analysis gave us a closer look at the micro-environment around the active sites and the adsorbent, which helped us rationalize the photocatalytic performance of each sample in the next section.

### 3.4. In-Situ DRIFT Investigation of Photothermal $\text{CO}_2$ Reduction

The mechanisms of  $\text{CO}_2$  reduction and resultant intermediate products were monitored by in-situ DRIFT analysis. Figure 6a shows the time-dependent DRIFT absorbance spectra of  $\text{Pd}_2\text{Cu}/\text{P25}$ . The pristine  $\text{Pd}_2\text{Cu}/\text{P25}$  shows peaks of around  $3500\text{--}3000\text{ cm}^{-1}$  and  $1320\text{ cm}^{-1}$  for the surface hydroxyl group (moisture). These surface hydroxyl groups were initially removed by thermal treatment at  $150\text{ }^\circ\text{C}$  for 20 min in a nitrogen atmosphere. After removing the moisture, the  $\text{CO}_2$  and gas-phase  $\text{H}_2\text{O}$  were passed into the drift cell at  $150\text{ }^\circ\text{C}$ . The spectra were collected in time intervals (t) of 20, 40, and 60 min in darkness

(absence of light) and in the presence of light. The peaks appearing at  $2346\text{ cm}^{-1}$  and  $3700\text{--}3500\text{ cm}^{-1}$  correspond to the  $\nu_3$  and  $\nu_3 + \nu_1$  stretching vibrations of adsorbed  $\text{CO}_2$ , respectively. Additionally, the monodentate carbonate  $\text{CO}_3^{2-}$  peak appeared at  $1085\text{ cm}^{-1}$  for the metal carbonate (m-C-O-) [18], which confirmed the  $\text{CO}_2$  adsorption on  $\text{Pd}_2\text{Cu}/\text{P25}$  in dark.

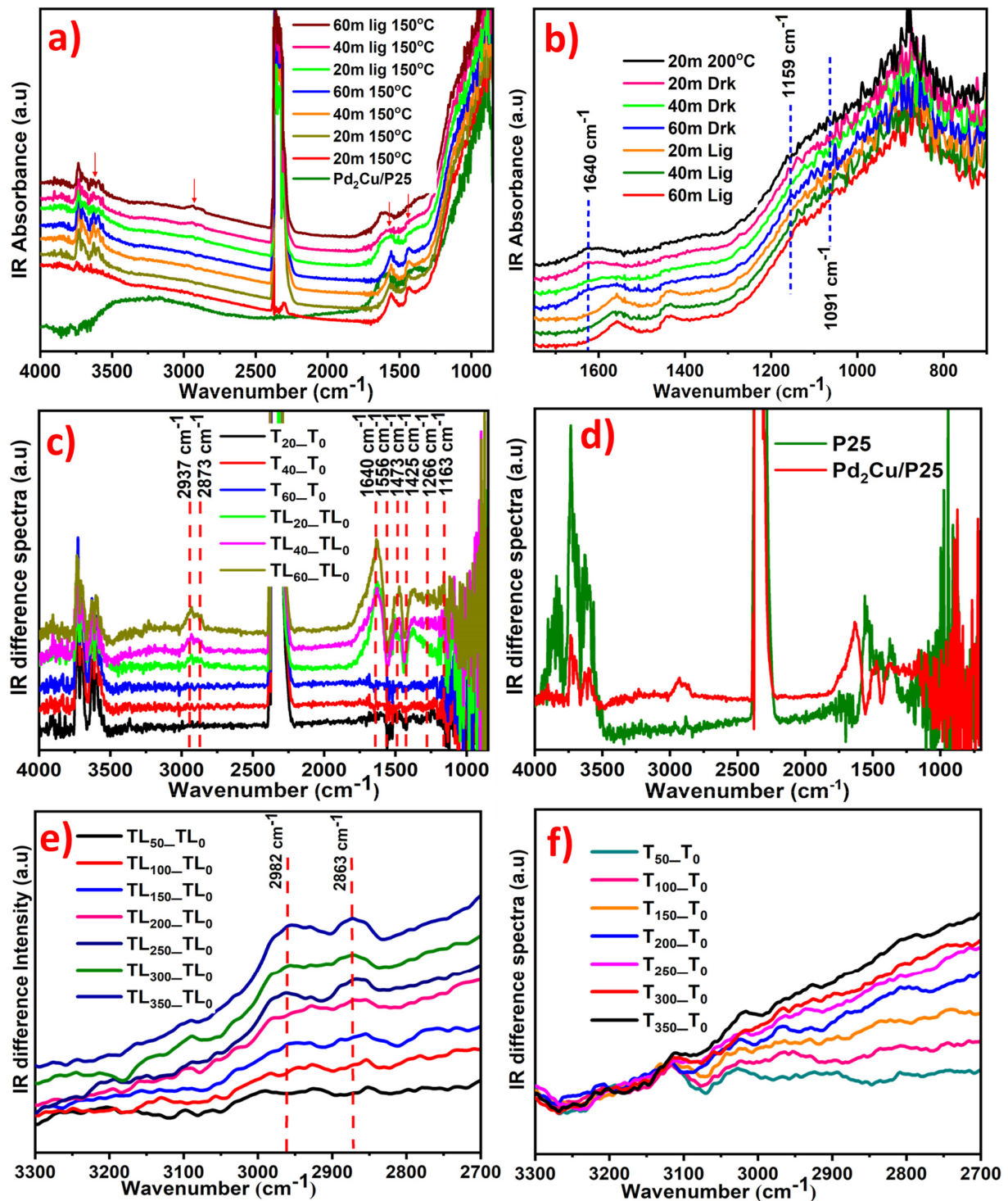


**Figure 6.** (a,b) Time-dependent DRIFT spectra of  $\text{Pd}_2\text{Cu}/\text{P25}$  and (c) IR difference spectra of  $\text{CO}_2$  reduction on  $\text{Pd}_2\text{Cu}/\text{P25}$ . (d) IR difference spectra of P25 and  $\text{Pd}_2\text{Cu}/\text{P25}$  after 1 h light irradiation. DRIFT spectra  $\text{CO}_2$  reduction on  $\text{Pd}_2\text{Cu}/\text{P25}$  at various temperatures (e) with and (f) without light irradiation.

This metal carbonate (m-C-O-) peak and the CO<sub>2</sub> peaks (3700–3500 cm<sup>-1</sup>) were slowly decreased when irradiated with UV-Vis light, and at the same time, the C-H peaks are increased at 2962 cm<sup>-1</sup> (Figure 6a). In addition, the \*CO peak arises at 1640 cm<sup>-1</sup> during the light irradiation, as shown in Figure 6b [19]. The obtained DRIFT spectra were derived to visualize the significant changes. Thereby, the obtained IR spectra were subtracted from the initial absorbance spectra. The T<sub>0</sub>, T<sub>20</sub>, T<sub>40</sub>, and T<sub>60</sub> refer to the spectra taken in darkness at t = 20, 40, and 60 min respectively. Similarly, TL<sub>0</sub>, TL<sub>20</sub>, TL<sub>40</sub>, and TL<sub>60</sub> refer to the spectra under UV-Vis light irradiation at t = 20, 40, and 60 min respectively. As shown in Figure 6c, the specific peaks at 2937, 2873 cm<sup>-1</sup> (asymmetric and symmetric C-H stretching frequency), and 3250 cm<sup>-1</sup> (-OH symmetric stretching) are increased with the reaction time [48–50]. The strong peaks at 1640 and 1473 cm<sup>-1</sup> were also increased, which correspond to the \*CO and CH<sub>2</sub> (scissoring), respectively. The small peaks at 1266 and 1163 cm<sup>-1</sup> refer to the formation of C-C (stretching frequency) and CO<sub>2</sub><sup>δ-</sup>, respectively [19]. The peaks at 1556 and 1425 cm<sup>-1</sup> correspond to the CO<sub>3</sub><sup>2-</sup> and CHCOH respectively. These two peaks are gradually decreased by further increasing the reaction time. From these observations, we have illustrated the mechanistic pathway of CO<sub>2</sub> reduction given below.



In the above reaction steps, the CO<sub>2</sub> gas-phase is adsorbed as a monodentate metal carbonate (m-C-O-) CO<sub>3</sub><sup>2-</sup>. On the catalytic (Cu) surface, the CO<sub>3</sub><sup>2-</sup> to \*CO conversion occurs via π-π interaction by the excited electrons [46]. The local concentration of CO on the catalyst (Pd) undergoes the C-C coupling step, and then the OC-CO reacts with water and produces the intermediates of CHCOH. Furthermore, the addition of water with CHCOH produces the final product of ethanol [18]. Overall, DRIFT studies have demonstrated the reaction pathways wherein Cu was assumed as a CO<sub>2</sub> adsorption site. It is very difficult to separate the active sites in DRIFT spectra where the CO<sub>2</sub> is adsorbed. However, previous studies have demonstrated that CO<sub>2</sub> adsorption is more favorable on the Cu site [25].

On other hand, Pd was engaged in the C-C coupling reaction, as well as the highly selective hydrogenation of CO<sub>2</sub> to C<sub>2</sub>H<sub>5</sub>OH. The production of ethanol was confirmed by the mass spectra. The CO<sub>2</sub> reduction on Pd<sub>2</sub>Cu/P25 was compared with P25. The corresponding DRIFT results are shown in Figure 6d. Hence, the Pd<sub>2</sub>Cu/P25 is a more selective and active catalyst that produces ethanol when compared to P25. Moreover, the photothermal hydrogenation of CO<sub>2</sub> over the Pd<sub>2</sub>Cu/P25 catalyst was evaluated at various temperatures under UV-Vis light irradiation (Figure 6e). The DRIFT difference spectra reveal that the C<sub>2</sub>H<sub>5</sub>OH formation (identified from C-H peaks arising) increased with an increase in temperature. In contrast, the reaction was continued without light irradiation at 150 °C, exhibiting no C-H peak, and with no ethanol formation in dark (Figure 6f). Therefore, the light provides the driving force for CO<sub>2</sub> reduction (0.611 V) and water oxidation (1.23 V). Overall, the reaction begins with the oxidation of water on P25 and then the electrons that evolved during water oxidation are utilized by Pd<sub>2</sub>Cu. The H<sub>2</sub> molecules are generated from the P25 as a result of photocatalytic water oxidation. The Cu provides the active site for CO<sub>2</sub> adsorption and Pd oxidizes the generated H<sub>2</sub> molecules and involves the C-C bond formation. The key step of the CO<sub>2</sub> reduction is the hydrogenation of \*CO to \*HCO, which is performed by the Pd active sites.

#### 4. Conclusions

This work reports the photothermal reduction of CO<sub>2</sub> and the oxidation of H<sub>2</sub>O over the Pd<sub>2</sub>Cu/P25 photocatalyst. The formation of ethanol was confirmed from GCMS and on-line mass spectroscopy. The Pd<sub>2</sub>Cu/P25 showed an efficient CO<sub>2</sub> reduction photothermally at 150 °C with an ethanol production rate of 4.1 mmol g<sup>-1</sup> h<sup>-1</sup> under UV-Vis irradiation. Other products were not visible on GCMS spectra due to their low quantity. However, operando DRIFT absorption spectroscopy traces the intermediate products. The mechanism

of CO<sub>2</sub> reduction on the Pd<sub>2</sub>Cu/P25 catalyst was monitored by DRIFTS. The reaction begins with the oxidation of water on P25 and then the electrons involved in water oxidation were utilized by Pd<sub>2</sub>Cu. The Pd active sites utilize those electrons and hydrogenate the \*CO to \*HCO, which is a key step for the reduction of CO<sub>2</sub> to ethanol. Moreover, the Pd<sub>2</sub>Cu/P25 catalyst demonstrated the highly active and selective hydrogenation of CO<sub>2</sub> to C<sub>2</sub>H<sub>5</sub>OH.

**Author Contributions:** Conceptualization, M.E. and T.C.-K.Y.; methodology, M.E. and W.Y.; software, M.E. and W.Y.; validation, W.Y., S.V. and J.-N.C.; formal analysis, S.V. and J.-N.C.; investigation, S.V. and J.-N.C.; resources, T.C.-K.Y. and T.Y.; data curation, M.E., S.V. and J.-N.C.; writing—original draft preparation, M.E., W.Y. and S.V.; writing—review and editing, S.V., T.C.-K.Y. and T.Y.; visualization, M.E., W.Y. and S.V.; supervision, T.C.-K.Y. and T.Y.; project administration, T.C.-K.Y., funding acquisition, T.C.-K.Y. All authors have read and agreed to the published version of the manuscript.

**Funding:** The authors would like to acknowledge partial financial support from the Taiwan Ministry of Science and Technology with project number 110-2221-E-027-006-MY2.

**Institutional Review Board Statement:** Not applicable.

**Informed Consent Statement:** Not applicable.

**Data Availability Statement:** Data are contained within the article.

**Acknowledgments:** The authors express gratitude to Precision Analysis and Material Research Center, National Taipei University of Technology, Taipei, Taiwan for providing instrumental facilities.

**Conflicts of Interest:** The authors declare no conflict of interest.

## References

1. Yoon, Y.; Hall, A.S.; Surendranath, Y. Tuning of silver catalyst mesostructure promotes selective carbon dioxide conversion into fuels. *Angew. Chem. Int. Ed.* **2016**, *55*, 15282–15286. [[CrossRef](#)] [[PubMed](#)]
2. Rodemerck, U.; Holeña, M.; Wagner, E.; Smejkal, Q.; Barkschat, A.; Baerns, M. Catalyst development for CO<sub>2</sub> hydrogenation to fuels. *ChemCatChem* **2013**, *5*, 1948–1955. [[CrossRef](#)]
3. Behrens, M. Promoting the Synthesis of Methanol: Understanding the requirements for an industrial catalyst for the conversion of CO<sub>2</sub>. *Angew. Chem. Int. Ed.* **2016**, *55*, 14906–14908. [[CrossRef](#)]
4. Behrens, M. Heterogeneous catalysis of CO<sub>2</sub> conversion to methanol on copper surfaces, *Angew. Chem. Int. Ed.* **2014**, *53*, 12022–12024. [[CrossRef](#)] [[PubMed](#)]
5. Robatjazi, H.; Zhao, H.; Swearer, D.F.; Hogan, N.J.; Zhou, L.; Alabastri, A.; McClain, M.J.; Nordlander, P.; Halas, N.J. Plasmon-induced selective carbon dioxide conversion on earth-abundant aluminum–cuprous oxide antenna-reactor nanoparticles. *Nat. Commun.* **2017**, *8*, 27. [[CrossRef](#)]
6. Wang, W.; Wang, S.; Ma, X.; Gong, J. Recent advances in catalytic hydrogenation of carbon dioxide. *Chem. Soc. Rev.* **2011**, *4*, 3703–3727. [[CrossRef](#)]
7. Klankermayer, J.; Wesselbaum, S.; Beydoun, K.; Leitner, W. Selective catalytic synthesis using the combination of carbon dioxide and hydrogen: Catalytic chess at the interface of energy and chemistry. *Angew. Chem. Int. Ed.* **2016**, *55*, 7296–7343. [[CrossRef](#)] [[PubMed](#)]
8. Lu, Q.; Rosen, J.; Zhou, Y.; Hutchings, G.S.; Kimmel, Y.C.; Chen, J.G.; Jiao, F. A selective and efficient electrocatalyst for carbon dioxide reduction. *Nat. Commun.* **2014**, *5*, 3242. [[CrossRef](#)]
9. Kwak, J.H.; Kovarik, L.; Szanyi, J. Photocatalytic reduction of CO<sub>2</sub> on TiO<sub>2</sub> and other semiconductors, CO<sub>2</sub> reduction on supported Ru/Al<sub>2</sub>O<sub>3</sub> catalysts: Cluster size dependence of product selectivity. *ACS Catal.* **2013**, *3*, 2449–2455. [[CrossRef](#)]
10. Porosoff, M.D.; Yang, X.; Boscoboinik, J.A.; Chen, J.G. Molybdenum carbide as alternative catalysts to precious metals for highly selective reduction of CO<sub>2</sub> to CO. *Angew. Chem. Int. Ed.* **2014**, *53*, 6705–6709. [[CrossRef](#)]
11. Martin, O.; Martín, A.J.; Mondelli, C.; Mitchell, S.; Segawa, T.F.; Hauert, R.; Drouilly, C.; Curulla-Ferré, D.; Pérez-Ramírez, J. Indium oxide as a superior catalyst for methanol synthesis by CO<sub>2</sub> hydrogenation. *Angew. Chem. Int. Ed.* **2016**, *55*, 6261–6265. [[CrossRef](#)]
12. Studt, F.; Sharafutdinov, I.; Abild-Pedersen, F.; Elkjær, C.F.; Hummelshøj, J.S.; Dah, S.; Chorkendorff, I.; Nørskov, J.K. Discovery of a Ni-Ga catalyst for carbon dioxide reduction to methanol. *Nat. Chem.* **2014**, *6*, 320–324. [[CrossRef](#)] [[PubMed](#)]
13. Graciani, J.; Mudiyansele, K.; Xu, F.; Baber, A.E.; Evans, J.; Senanayake, S.D.; Stacchiola, D.J.; Liu, P.; Hrbek, J.; Sanz, J.F.; et al. Highly active copper-ceria and copper-ceria-titania catalysts for methanol synthesis from CO<sub>2</sub>. *Science* **2014**, *345*, 546–550. [[CrossRef](#)] [[PubMed](#)]
14. Moret, S.; Dyson, P.J.; Laurenczy, G. Direct synthesis of formic acid from carbon dioxide by hydrogenation in acidic media. *Nat. Commun.* **2014**, *5*, 4017. [[CrossRef](#)] [[PubMed](#)]

15. Zhu, Y.; Zhang, S.; Ye, Y.; Zhang, X.; Wang, L.; Zhu, W.; Cheng, F.; Tao, F. Catalytic conversion of carbon dioxide to methane on Ruthenium-Cobalt bimetallic nanocatalysts and correlation between surface chemistry of catalysts under reaction conditions and catalytic performances. *ACS Catal.* **2012**, *2*, 2403–2408. [[CrossRef](#)]
16. Mistry, H.; Varela, A.S.; Bonifacio, C.S.; Zegkinoglou, I.; Sinev, I.; Choi, Y.-W.; Kisslinger, K.; Stach, E.A.; Yang, J.C.; Strasser, P.; et al. Highly selective plasma-activated copper catalysts for carbon dioxide reduction to ethylene. *Nat. Commun.* **2016**, *7*, 12123. [[CrossRef](#)]
17. Choi, Y.H.; Jang, Y.J.; Park, H.; Kimb, W.Y.; Lee, Y.H.; Choi, S.H.; Lee, J.S. Carbon dioxide Fischer–Tropsch synthesis: A new path to carbon-neutral fuels. *Appl. Catal. B Environ.* **2017**, *202*, 605–610. [[CrossRef](#)]
18. Li, F.; Li, Y.C.; Wang, Z.; Li, J.; Nam, D.-H.; Lum, Y.; Luo, M.; Wang, X.; Ozden, A.; Hung, S.-F.; et al. Cooperative CO<sub>2</sub>-to-ethanol conversion via enriched intermediates at molecule–metal catalyst interfaces. *Nat. Catal.* **2020**, *3*, 75–82. [[CrossRef](#)]
19. Bai, S.; Shao, Q.; Wang, P.; Dai, Q.; Wang, X.; Huang, X. Highly Active and Selective Hydrogenation of CO<sub>2</sub> to Ethanol by Ordered Pd–Cu Nanoparticles. *J. Am. Chem. Soc.* **2017**, *139*, 6827–6830. [[CrossRef](#)]
20. Qian, C.; Sun, W.; Hung, D.L.H.; Qiu, C.; Makarem, M.; Kumar, S.G.H.; Wan, L.; Ghossoub, M.; Wood, T.E.; Xia, M.; et al. Catalytic CO<sub>2</sub> reduction by palladium-decorated silicon–hydride nanosheets. *Nat. Catal.* **2019**, *2*, 46–54. [[CrossRef](#)]
21. Fujitani, T.; Nakamura, I. Methanol Synthesis from CO and CO<sub>2</sub> Hydrogenations over Supported Palladium Catalysts. *Bull. Chem. Soc. Jpn.* **2002**, *75*, 1393–1398. [[CrossRef](#)]
22. Crudden, C.M.; Sateesh, M.; Lewis, R. Mercaptopropyl-modified mesoporous silica: Remarkable support for the preparation of a reusable, heterogeneous palladium catalyst for coupling reactions. *J. Am. Chem. Soc.* **2005**, *127*, 10045–10050. [[CrossRef](#)]
23. Pang, S.H.; Schoenbaum, C.A.; Schwartz, D.K.; Medlin, J.W. Directing reaction pathways by catalyst active-site selection using self-assembled monolayers. *Nat. Commun.* **2013**, *4*, 2448. [[CrossRef](#)] [[PubMed](#)]
24. Lee, G.-J.; Anandan, S.; Masten, S.J.; Wu, J.J. Photocatalytic hydrogen evolution from water splitting using Cu doped ZnS microspheres under visible light irradiation. *Renew. Energy* **2016**, *89*, 2619. [[CrossRef](#)]
25. Imtiaz, Q.; Yüzbaşı, N.S.; Abdala, P.M.; Kierzkowska, A.M.; Beek, W.V.; Brodaa, M.; Müller, C.R. Development of MgAl<sub>2</sub>O<sub>4</sub>-stabilized, Cu-doped, Fe<sub>2</sub>O<sub>3</sub>-based oxygen carriers for thermochemical water-splitting. *J. Mater. Chem. A* **2016**, *4*, 113–123. [[CrossRef](#)]
26. Hunge, Y.M.; Yadav, A.A.; Mathe, V.L. Photocatalytic hydrogen production using TiO<sub>2</sub> nanogranules prepared by hydrothermal route. *Chem. Phys. Lett.* **2019**, *731*, 136582. [[CrossRef](#)]
27. Gosavi, S.; Tabei, R.; Roy, N.; Latthe, S.S.; Hunge, Y.M.; Suzuki, N.; Kondo, T.; Yuasa, M.; Teshima, K.; Fujishima, A.; et al. Low Temperature Deposition of TiO<sub>2</sub> Thin Films through Atmospheric Pressure Plasma Jet Processing. *Catalysts* **2021**, *11*, 91. [[CrossRef](#)]
28. Chen, Y.-W.; Hsu, Y.-H. Effects of reaction temperature on the photocatalytic activity of TiO<sub>2</sub> with Pd and Cu cocatalysts. *Catalysts* **2021**, *11*, 966. [[CrossRef](#)]
29. Lohumi, S.; Lee, S.; Lee, H.; Cho, B.K. A review of vibrational spectroscopic techniques for the detection of food authenticity and adulteration. *Trends Food Sci. Technol.* **2015**, *46*, 85–98. [[CrossRef](#)]
30. Manju, G.; Archana, J.; Verma, K.K. Dispersive liquid–liquid microextraction and diffuse reflectance-Fourier transform infrared spectroscopy for iodate determination in food grade salt and food samples. *Food Chem.* **2022**, *368*, 130810.
31. Elavarasan, M.; Uma, K.; Yang, T.C.-K. Photocatalytic oxidation of ethanol using ultrasonic modified TiO<sub>2</sub>; an in-situ diffuse reflectance infrared spectroscopy study. *Results Phys.* **2019**, *13*, 1022372. [[CrossRef](#)]
32. Yang, T.C.-K.; Wang, S.-F.; Tsai, S.H.-Y.; Lin, S.-Y. Intrinsic photocatalytic oxidation of the dye adsorbed on TiO<sub>2</sub> photocatalysts by diffuse reflectance infrared Fourier transform spectroscopy. *Appl. Catal. B Environ.* **2001**, *30*, 293–301. [[CrossRef](#)]
33. Liu, J.; Winwarid, P.; Yang, T.C.-K.; Chuang, S.S.-C. In situ infrared study of photo-generated electrons and adsorbed species on nitrogen-doped TiO<sub>2</sub> in dye-sensitized solar cells. *Phys. Chem. Chem. Phys.* **2018**, *20*, 19572–19580. [[CrossRef](#)]
34. Xu, F.; Meng, K.; Cheng, B.; Yu, J.; Ho, W. Enhanced Photocatalytic Activity and Selectivity for CO<sub>2</sub> Reduction over a TiO<sub>2</sub> Nanofiber Mat Using Ag and MgO as Bi-Cocatalyst. *ChemCatChem.* **2019**, *11*, 465–472. [[CrossRef](#)]
35. Yang, Q.; Le, X.; Li, Y.; Ian, T.M.; Guo, F.; Tao, M.; Yang, R.; Qi, L.; Lin, Z.; Gu, S.; et al. BCC-Phased PdCu Alloy as a Highly Active Electrocatalyst for Hydrogen Oxidation in Alkaline Electrolytes. *J. Am. Chem. Soc.* **2018**, *140*, 16580–16588.
36. Gu, Z.; Xiong, Z.; Ren, F.; Li, S.; Xu, H.; Yan, B.; Du, Y. Flower-like PdCu catalyst with high electrocatalytic properties for ethylene glycol oxidation. *J. Taiwan Inst. Chem. E* **2018**, *83*, 32–39. [[CrossRef](#)]
37. Tiscione, N.B.; Alford, I.; Yeatman, D.T.; Shan, X. Ethanol Analysis by Headspace Gas Chromatography with Simultaneous Flame-Ionization and Mass Spectrometry Detection. *J. Anal. Toxicol.* **2011**, *35*, 501–511. [[CrossRef](#)]
38. He, Z.; Qian, Q.; Ma, J.; Meng, Q.; Zhou, H.; Song, J.; Liu, Z.; Han, B. Water-enhanced synthesis of higher alcohols from CO<sub>2</sub> hydrogenation over a Pt/Co<sub>3</sub>O<sub>4</sub> catalyst under Milder conditions, *Angew. Chem. Int. Ed.* **2016**, *55*, 737–741. [[CrossRef](#)]
39. Pan, X.; Fan, Z.; Chen, W.; Ding, Y.; Luo, H.; Bao, X. Enhanced ethanol production inside carbon-nanotube reactors containing catalytic particles. *Nat. Mater.* **2007**, *6*, 507–511. [[CrossRef](#)] [[PubMed](#)]
40. Yang, N.; Medford, A.J.; Liu, X.; Studt, F.; Bligaard, T.; Bent, S.F.; Nørskov, J.K. Intrinsic selectivity and structure sensitivity of rhodium catalysts for C<sub>2+</sub> oxygenate production. *J. Am. Chem. Soc.* **2016**, *138*, 3705–3714. [[CrossRef](#)]
41. Wang, D.; Bi, Q.; Yin, G.; Zhao, W.; Huang, F.; Xie, X.; Jiang, M. Direct synthesis of ethanol via CO<sub>2</sub> hydrogenation using supported gold catalysts. *Chem. Commun.* **2016**, *52*, 14226–14229. [[CrossRef](#)] [[PubMed](#)]

42. Jiang, X.; Koizumi, N.; Guo, X.; Song, C. Bimetallic Pd–Cu catalysts for selective CO<sub>2</sub> hydrogenation to methanol. *Appl. Catal. B Environ.* **2015**, *170*, 173–185. [[CrossRef](#)]
43. Baltrusaitis, J.; Jensen, J.H.; Grassian, V.H. FTIR spectroscopy combined with isotope labeling and quantum chemical calculations to investigate adsorbed bicarbonate formation following reaction of carbon dioxide with surface hydroxyl groups on Fe<sub>2</sub>O<sub>3</sub> and Al<sub>2</sub>O<sub>3</sub>. *J. Phys. Chem. B* **2006**, *110*, 12005–12016. [[CrossRef](#)]
44. Turek, A.M.; Wachs, I.E.; DeCanio, E. Acidic properties of alumina-supported metal oxide catalysts: An infrared spectroscopy study. *J. Phys. Chem. B* **1992**, *96*, 5000–5007. [[CrossRef](#)]
45. Collins, S.E.; Baltanás, M.A.; Bonivardi, A.L. Infrared spectroscopic study of the carbon dioxide adsorption on the surface of Ga<sub>2</sub>O<sub>3</sub> polymorphs. *J. Phys. Chem. B* **2006**, *110*, 5498–5507. [[CrossRef](#)]
46. Collins, S.E.; Baltanas, M.A.; Bonivardi, A.L. An infrared study of the intermediates of methanol synthesis from carbon dioxide over Pd/ $\beta$ -Ga<sub>2</sub>O<sub>3</sub>. *J. Catal.* **2004**, *226*, 410–421. [[CrossRef](#)]
47. Köck, E.M.; Kogler, M.; Bielez, T.; Klötzer, B.; Penner, S. In situ FT-IR spectroscopic study of CO<sub>2</sub> and CO adsorption on Y<sub>2</sub>O<sub>3</sub>, ZrO<sub>2</sub>, and yttria-stabilized ZrO<sub>2</sub>. *J. Phys. Chem. C* **2013**, *117*, 17666–17673.
48. Yu, Z.; Chuang, S.S.C. In situ IR study of adsorbed species and photo-generated electrons during photocatalytic oxidation of ethanol on TiO<sub>2</sub>. *J. Catal.* **2007**, *246*, 118–126. [[CrossRef](#)]
49. Elavarasan, M.; Uma, K.; Yang, T.C.-K. Nanocubes phase adaptation of In<sub>2</sub>O<sub>3</sub>/TiO<sub>2</sub> heterojunction photocatalysts for the dye degradation and tracing of adsorbed species during photo-oxidation of ethanol. *J. Taiwan Inst. Chem. E* **2021**, *120*, 1–9. [[CrossRef](#)]
50. Guzman, F.; Chuang, S.S.C. Tracing the Reaction Steps Involving Oxygen and IR Observable Species in Ethanol Photocatalytic Oxidation on TiO<sub>2</sub>. *J. Am. Chem. Soc.* **2010**, *132*, 1502–1503. [[CrossRef](#)] [[PubMed](#)]